Environmental Science & Technology

pubs.acs.org/est

Article

Nanoscale Insights into the Interaction Mechanism Underlying the Adsorption and Retention of Heavy Metal Ions by Humic Acid

Zhoujie Wang, Qiuyi Lu, Chaopeng Liu, Huadong Tian, Jingyi Wang, Lei Xie,* Qi Liu, and Hongbo Zeng*

Cite This: *Environ. Sci. Technol.* 2024, 58, 3412−3422

Read Online

ACCESS | Metrics & More | Article Recommendations | Supporting Information

ABSTRACT: The mobility and distribution of heavy metal ions (HMs) in aquatic environments are significantly influenced by humic acid (HA), which is ubiquitous. A quantitative understanding of the interaction mechanism underlying the adsorption and retention of HMs by HA is of vital significance but remains elusive. Herein, the interaction mechanism between HA and different types of HMs (i.e., Cd(II), Pb(II), arsenate, and chromate) was quantitatively investigated at the nanoscale. Based on quartz crystal microbalance with dissipation tests, the adsorption capacities of Pb(II), Cd(II), As(V), and Cr(VI) ionic species on the HA surface were measured as ∼0.40, ∼0.25, ∼0.12, and ∼0.02 nmol cm^{-2}, respectively. Atomic force microscopy force results showed that the presence of Pb(II)/Cd(II) cations suppressed the electrostatic double-layer repulsion during the approach of two HA surfaces and the adhesion energy during separation was considerably enhanced from ∼2.18 to ∼5.05/∼4.18 mJ m^{-2}. Such strong adhesion stems from the synergistic metal−HA complexation and cation−π interaction, as evidenced by spectroscopic analysis and theoretical simulation. In contrast, As(V)/Cr(VI) oxo-anions could form only weak hydrogen bonds with HA, resulting in similar adhesion energies for HA−HA (∼2.18 mJ m^{-2}) and HA−As(V)/Cr(VI)−HA systems (∼2.26/∼1.96 mJ m^{-2}). This work provides nanoscale insights into quantitative HM−HA interactions, improving the understanding of HMs biogeochemical cycling.

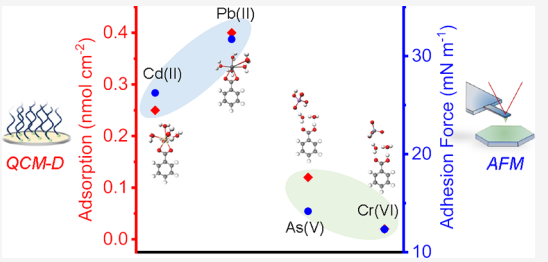

KEYWORDS: *heavy metal ions, humic acid, binding energy, atomic force microscope (AFM), QCM-D adsorption, DFT simulation*

1. INTRODUCTION

Heavy metals such as cadmium (Cd), lead (Pb), arsenic (As), and chromium (Cr) pose a severe threat to human and ecological health.[1] In aquatic environments, Cd and Pb are commonly present in the form of cationic Cd(II) and Pb(II) while As and Cr mainly exist as oxo-anion species (e.g., arsenate and chromate anions).[2,3] Although these heavy metal ions (HMs) are present in only trace amounts, they are considered some of the most toxic types of contaminants.[4,5] The mobility and distribution of HMs are intimately related to their ecological hazards,[6] and even a slow transport of HMs through the soil layer could result in pollution in groundwater.[7] Hence, considerable effort has been devoted to understanding the environmental fate and transport behaviors of HMs.[8,9] Natural organic matter (NOM) is an important component of organic carbon sinks in terrestrial and aquatic environments. Typically, NOM has a complex molecular structure with a variety of functional groups, such as carboxyl, hydroxyl, phenol, and amine, which enable versatile intermolecular interactions with HMs. The HM−NOM interactions dictate the adsorption and retention of HMs by NOM, which further governs the reactivity, bioavailability, toxicity, and transport of HMs within a diverse range of geochemical and environmental systems[10] and plays a critical role in the fate of both organic and inorganic compounds associated with the global carbon cycle.[11] Therefore, it is of great environmental significance to understand the interaction mechanism between the NOM and different types of HMs.

Over the past several decades, the interaction mechanisms between NOM and HMs have been investigated using advanced analytical techniques, including fluorescence spectroscopy,[12,13] attenuated total reflectance Fourier transform infrared (ATR-FTIR) spectroscopy,[14−16] and extended X-ray absorption fine structure (EXAFS).[17−19] Despite the significant progress achieved, most studies on the HM−NOM interactions were based on empirical or qualitative spectroscopic analysis. To date, the quantitative investigation of the interaction mechanism underlying the adsorption and retention of HMs by NOM, particularly at the nanoscale, remains challenging.

Received: October 7, 2023
Revised: January 5, 2024
Accepted: January 8, 2024
Published: January 22, 2024

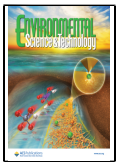

Atomic force microscopy (AFM) has been employed to quantitatively measure the intermolecular interactions between NOM and a variety of surfaces in complex aqueous systems at the nanoscale.[20−28] Based on chemical force microscopy (CFM), the intermolecular forces of humic acid (HA, a representative class of NOM, typical molecular structure as shown in Figure S1) interacting with monolayered surfaces of various well-defined chemical groups were quantitatively measured, which helped develop an efficient strategy for reversible adsorption and release of HA.[25] Recently, the interaction forces between HA-functionalized AFM probes and HA surfaces were quantified in aqueous environments containing NaCl or different types of divalent cations, which unraveled the complex aggregation mechanism of HA at the molecular level.[24,27] By quantitative investigation of the intermolecular interactions of HA−HM−HA systems, the binding mechanism of HA with different types of HMs could be deciphered at the nanoscale. Moreover, quartz crystal microbalance with dissipation (QCM-D) is a unique technique to monitor the mass change of adsorbed layer *in situ* and in real time,[29,30] which could provide quantitative information on the adsorption and retention of HMs on the HA surface. To the best of our knowledge, a quantitative study on the interaction mechanism of HA with HMs at the nanoscale has been rarely reported.

In this study, the interaction mechanism between HA and different types of HMs (i.e., Cd(II) and Pb(II) cations, arsenate, and chromate anions) was systemically investigated. The adsorption and retention of HMs on HA surfaces were monitored *in situ* using QCM-D, and the intermolecular forces and adhesion energies between HA-functionalized AFM probes and HA surfaces in the presence of different types of HMs were quantitatively measured at the nanoscale. The adsorption of HMs on HA surfaces is expected to induce bridging of HA−HM−HA, thereby enhancing interfacial adhesion. In addition, the morphology of HA surfaces in the presence of different types of HMs was imaged by AFM, and spectroscopic techniques and density functional theory (DFT) simulation were coupled to provide useful information on the bonding between HMs and HA. This work provides quantitative insights into the interaction mechanism underlying the adsorption and retention of HMs by HA at the molecular level, which hold great promise for developing effective strategies to mediate the transport of HMs in terrestrial and aquatic environments.

2. MATERIALS AND METHODS

2.1. Materials. Cadmium nitrate tetrahydrate ($Cd(NO_3)_2 \cdot 4H_2O$, ACS reagent, ≥99%), lead nitrate ($Pb(NO_3)_2$, ACS reagent, ≥99%), sodium arsenate heptahydrate ($Na_2HAsO_4 \cdot 7H_2O$, ACS reagent, ≥98%), potassium dichromate ($K_2Cr_2O_7$, ACS reagent, ≥99%), sodium chloride (NaCl, ACS reagent, ≥99%), sodium nitrate ($NaNO_3$, ACS reagent, ≥99%), nitric acid solution (HNO_3, 100 mM), and sodium hydroxide (NaOH, ACS reagent, ≥97%) were obtained from Sigma-Aldrich. (3-Aminopropyl)triethoxysilane (APTES, $H_2N-(CH_2)_3Si(OC_2H_5)_3$, 99%), *N*-hydroxysuccinimide (NHS, $C_4H_5NO_3$, 98%), *N*-(3-(dimethylamino)propyl)-*N*′-ethylcarbodiimide hydrochloride (EDC, $C_8H_{17}N_3 \cdot HCl$, 98%), and HA (more details in the Supporting Information) were purchased from Aladdin Biochemical Technology. All of the chemicals were used as received without further purification. Milli-Q water (Millipore deionized) with a resistance of >18.2 MΩ·cm at 25 °C was used in all the experiments, and NaOH and HNO_3 were used as pH regulators. All of the experiments were performed at a typical environmental pH (∼5.8).

2.2. QCM-D Measurement. A QCM-D (Q-Sense E4, Biolin Scientific) was used to monitor the *in situ* adsorption of HMs on silica sensors without or with a HA coating. Silica sensors coated with HA layers were prepared following the previous protocol.[27] For each adsorption experiment, a 1 mM HMs solution was adjusted to pH 5.8 and the temperature was stabilized at 25 °C. Prior to the adsorption experiment, HA-coated sensors were exposed to Milli-Q water until a stable baseline was recorded. The HMs solution was then introduced with a flow rate of 100 μL min^{-1} until the adsorption equilibrium of HMs was achieved. During the measurement, the change in the resonance frequency (f) of the QCM-D sensors was recorded with time and the negative/positive frequency shifts indicate the adsorption/release of HMs. The adsorption capacity was calculated using the composite Sauerbrey model (more details in the Supporting Information).

2.3. Surface Characterization. The elemental composition of HA was analyzed by using an organic elemental analyzer (vario EL Cube, Elementar Co.). The vibrational characteristics of HA before and after HMs treatment were analyzed by Fourier transform infrared spectroscopy (FTIR, Thermo Scientific Nicolet iS20). Briefly, the transmission FTIR mode was used in this work. The solution containing 1 mM HMs and 100 mM HA was stirred for several hours. Subsequently, the aggregates were filtered and dried in a vacuum oven at 40 °C for 48 h before promptly conducting the FTIR test. HA-coated surfaces for AFM imaging and XPS measurements were prepared following the previous protocol.[27] The freshly prepared HA surfaces were conditioned in 1 mM HMs solution at pH 5.8 for 30 min and then washed with Milli-Q water (pH 5.8), dried with high-purity nitrogen, and immediately used for AFM imaging and XPS measurements. An AFM instrument (MFP-3D Bio, Asylum Research) was used to characterize the morphology of HA surfaces adsorbed with different types of HMs. The XPS measurements were performed on a Thermo Scientific K-Alpha system (Thermo Fisher Scientific Inc., USA) equipped with an Al K_α X-ray source ($h\nu$ = 1486.6 eV) to unravel the HM−HA bonding information. Survey spectra were recorded in a single sweep from 0 to 1350 eV using a step size of 1.0 eV, while a step size of 0.1 eV was used for high-resolution scans. The C 1s peak at 284.8 eV (C−C) was used as the internal binding energy standard for calibration.

2.4. AFM Force Measurement. The interaction forces between HA-functionalized AFM probes and HA surfaces were measured in a 10 mM NaCl solution with or without 1 mM HMs at pH 5.8 to delineate the HM−HA or HA−HA interaction mechanism, respectively. The radius of the HA-functionalized AFM tip used in this work is consistent with our previous reports.[24,27] The detailed HA-functionalization protocol on AFM probes was developed following the previous protocol.[27] In a typical force measurement, the HA-functionalized AFM probe was driven to approach the HA surface at a loading force of 5 nN and a loading velocity of 0.5 μm s^{-1} and then to retract from the surface to complete a force−separation cycle. By scanning the AFM probe on the surface, force mapping (20 × 20 points on a 2 × 2 μm^2 region) was performed to acquire the two-dimensional arrays of force−separation profiles (400 consecutive force−separation cycles).

https://doi.org/10.1021/acs.est.3c08309
Environ. Sci. Technol. 2024, 58, 3412−3422

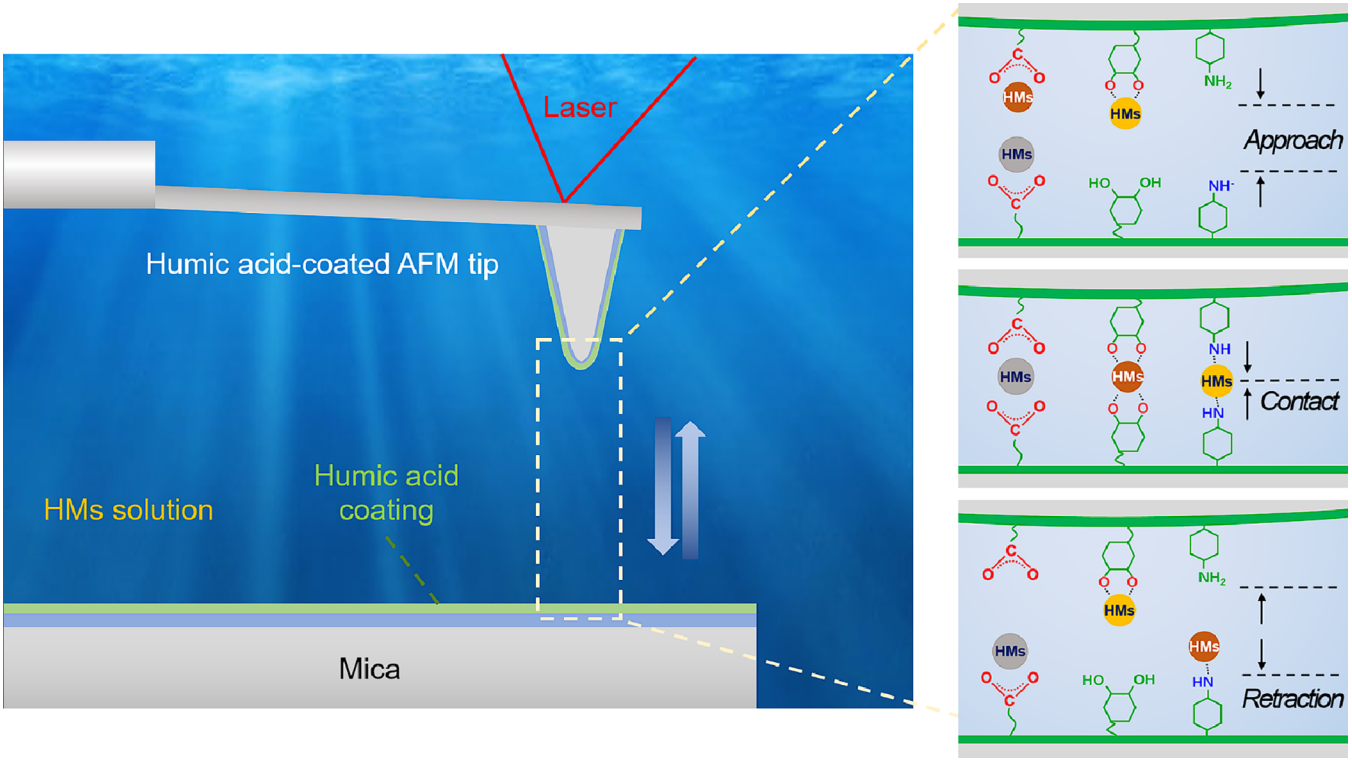

Figure 1. Schematic of the AFM setup for measuring the interaction forces between a HA-functionalized AFM probe and a HA-coated substrate in aqueous solution containing different types of HMs.

The deflection of the AFM cantilever was detected through a laser beam that was reflected from the cantilever into a split photodiode detector, which was further converted to the force using the spring constant and Hooke's law. The schematic of the AFM force measurement setup is illustrated in Figure 1.

2.5. Interpretation of Force–Separation Profiles. The AFM force–separation profiles measured during the approach can be explained by the classical Derjaguin–Landau–Verwey–Overbeek (DLVO) theory. The DLVO forces F_{DLVO} comprise van der Waals (vdW) force F_{vdW} and electrostatic double-layer (EDL) force F_{EDL}.

$$F_{vdW} = \frac{A_H}{6}\left(\frac{R + D - 2L}{L^2} - \frac{R - D}{D^2}\right) - \frac{A_H}{3\tan^2\alpha}\left(\frac{1}{L} + \frac{R\sin\alpha\tan\alpha - D - R(1 - \cos\alpha)}{2L^2}\right) \quad (1)$$

$$F_{EDL} = \frac{4\pi}{\varepsilon_0\varepsilon\kappa^2}\sigma_T\sigma_S(a_0e^{-\kappa D} - a_1e^{-\kappa L}) + \frac{2\pi}{\varepsilon_0\varepsilon\kappa^2}(\sigma_T^2 + \sigma_S^2)(a_2e^{-2\kappa D} - a_3e^{-2\kappa L}) + + \frac{4\pi}{\varepsilon_0\varepsilon\kappa\tan\alpha}[b_1\sigma_T\sigma_Se^{-\kappa L} + b_2\frac{\sigma_T^2 + \sigma_S^2}{2}e^{-2\kappa L}] \quad (2)$$

$$F_{DLVO} = F_{vdW} + F_{EDL} \quad (3)$$

where A_H, ε_0, ε, $1/\kappa$, and σ represent the nonretarded Hamaker constant, vacuum permittivity, dielectric constant of solution, Debye length, and surface charge density, respectively. The subscripts S and T refer to the substrate and tip, respectively. R, D, L, and α are the tip parameters, with the details in our previous work.[24,25]

$$a_0 = \kappa R - 1,\quad a_1 = \kappa R\cos\alpha - 1,\quad a_2 = a_0 + 0.5,\ \text{and}\quad a_3 = a_1 + 0.5 \quad (4)$$

$$b_1 = R\sin\alpha - \frac{D + R(1 - \cos\alpha)}{\tan\alpha} + \frac{1}{\tan\alpha}(L + \frac{1}{\kappa}) \quad (5)$$

$$b_2 = R\sin\alpha - \frac{D + R(1 - \cos\alpha)}{\tan\alpha} + \frac{1}{\tan\alpha}(L + \frac{1}{2\kappa}) \quad (6)$$

2.6. DFT Simulation. All of the simulation results were calculated using the DMol3 package implemented in Materials Studio 2019. The generalized gradient approximation (GGA), Perdew–Burke–Ernzerhof for the exchange-correlation potential, and double numerical basis sets including the p-polarization function (DNP) were used in our systems. The threshold values of convergence criterion were 10^{-5} Ha for energy, 0.002 Ha Å^{-1} for maximum force, 0.005 Å for maximum displacement, and 0.1 GPa for maximum stress. The vdW interaction was included by using the DFT-D method.

The binding energies (E_{ad}) for HM adsorption on optimized silica clusters and HA species were calculated according to eq 7:

$$E_{ad} = E_{(\text{Silica or HA species + adsorbed HMs})} - E_{(\text{Silica or HA species})} - E_{(HMs)} \quad (7)$$

where $E_{(\text{Silica or HA species + adsorbed HMs})}$ is the total energy, $E_{(\text{Silica or HA species})}$ is the energy of the optimized silica clusters or HA species, and $E_{(HMs)}$ is the energy of HMs.

https://doi.org/10.1021/acs.est.3c08309
Environ. Sci. Technol. 2024, 58, 3412–3422

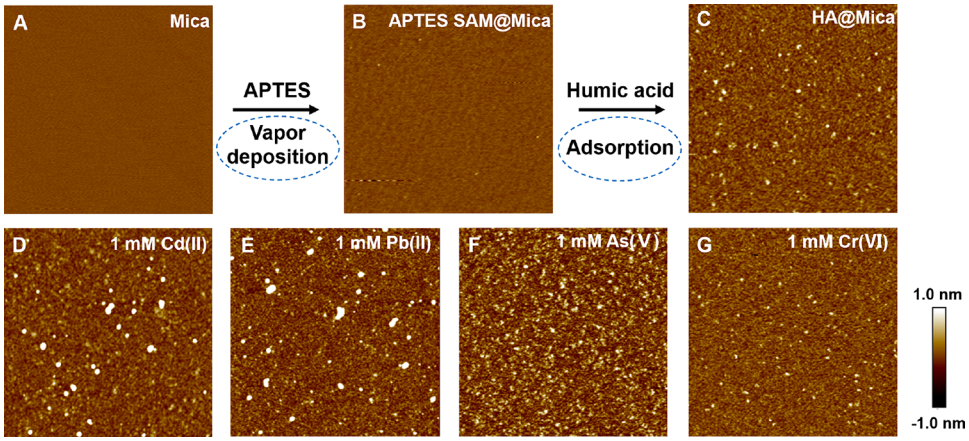

Figure 2. AFM topographic images ($2 \times 2\ \mu m^2$) of (A) bare mica, (B) APTES-functionalized mica, and (C) HA-coated mica surfaces, and AFM topographic images ($2 \times 2\ \mu m^2$) of HA surfaces in the presence of 1 mM HMs: (D) Cd(II), (E) Pb(II), (F) As(V), and (G) Cr(VI).

The net charge of atoms during HM adsorption was calculated as eq 8:

$$\text{net charge} = \text{Mulliken Charge}_{\text{after}} - \text{Mulliken Charge}_{\text{before}} \quad (8)$$

where $\text{Mulliken Charge}_{\text{after}}$ and $\text{Mulliken Charge}_{\text{before}}$ represent the charge of atoms after and before HMs adsorption, respectively. For the net charge, the positive value indicates the loss of electrons during the adsorption process.

3. RESULTS AND DISCUSSION

3.1. Morphology of HA Surfaces in the Presence of HMs. Figure 2A–C shows the topographic images of bare mica, APTES-functionalized mica, and HA-coated mica surfaces. The bare mica surface (Figure 2A) exhibits molecular smoothness with a root-mean-square (RMS) roughness of ~0.22 nm. The APTES-functionalized mica surface (Figure 2B) displays the morphology and RMS roughness (~0.25 nm) similar to the bare mica surface since the self-assembly of small molecules could not change the characteristic morphology of substrates. After HA adsorption, the APTES self-assembled monolayer surface is replaced by the grain-like morphology with few small aggregates and the RMS roughness increases to ~0.37 nm (Figure 2C). A typical film thickness of adsorbed HA film has been determined as ~12 nm based on repeatable measurements using surface forces apparatus in our previous work.[31] The bare mica, APTES-functionalized mica, and HA-coated mica surfaces show the water contact angles of <5, 47, and 42° (Figure S2), respectively, which further reveals the successful coating of HA on mica surface.

The morphology of HA surfaces after HMs adsorption is shown in Figure 2D–G. As illustrated in Figure 2D,E, the size of the HA aggregates formed considerably increases in the presence of Cd(II) and Pb(II), with the RMS roughness rising to ~0.64 and ~0.70 nm, respectively. This phenomenon mainly arises from the robust binding of cationic Cd(II) and Pb(II) with the deprotonated oxygen-containing functional groups (e.g., carboxyl and phenol groups) in HA molecules (Table S1), which leads to the bridging of HA molecules and the formation of HA aggregates.[32] In contrast, the size of HA aggregates in the presence of As(V) (Figure 2F) becomes much smaller (RMS roughness ~0.45 nm), which is attributed to the relatively weak bonding of anionic As(V) (viz., arsenate) with HA. In Figure 2G, the morphology of the HA surface in the presence of anionic Cr(VI) (viz., chromate, RMS roughness ~0.36 nm) is quite similar to that without HMs (Figure 2C), which indicates the negligible bonding of anionic Cr(VI) with HA molecules. Based on AFM imaging, it is clear that the cationic Cd(II) and Pb(II) exhibit the strongest bonding with HA molecules, followed by the anionic As(V), while the interaction of anionic Cr(VI) with HA molecules is negligible.

3.2. Binding Mechanism between HA and HMs. XPS is a surface-sensitive analytical technique to provide valuable information on HMs–HA bonding. Herein, bare silica and HA surfaces conditioned with different types of HMs were characterized by XPS. The high-resolution XPS spectra of Cd 3d, Pb 4f, As 3d, and Cr 2p in Figure 3 show that the

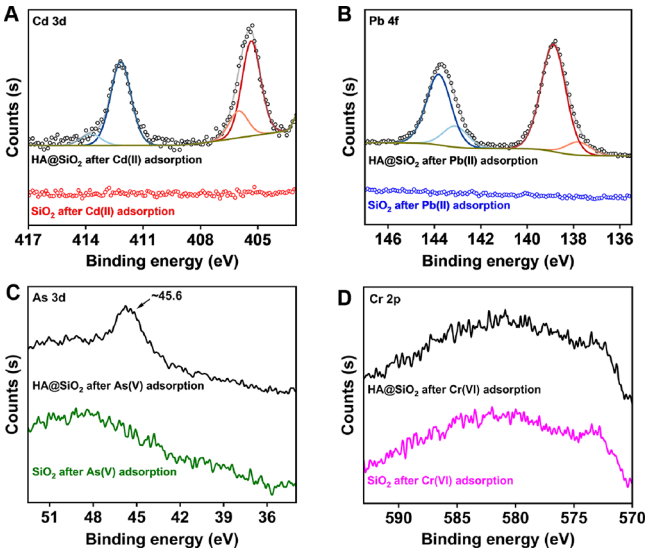

Figure 3. High-resolution XPS spectra of (A) Cd 3d, (B) Pd 4f, (C) As 3d, and (D) Cr 2p on bare silica and HA surfaces after the treatment of different HMs.

Cd(II), Pb(II), As(V), and Cr(VI) species are not detected on the bare silica surface, which indicates that HMs could not be retained by the silica surface. In contrast, HA surfaces after HM adsorption exhibit distinct XPS spectra. Typically, the Cd 3d spectrum (Figure 3A) displays the peaks at the binding energies of 405.3 and 406.0 eV for Cd 3d 5/2 as well as 412.3

https://doi.org/10.1021/acs.est.3c08309
Environ. Sci. Technol. 2024, 58, 3412–3422

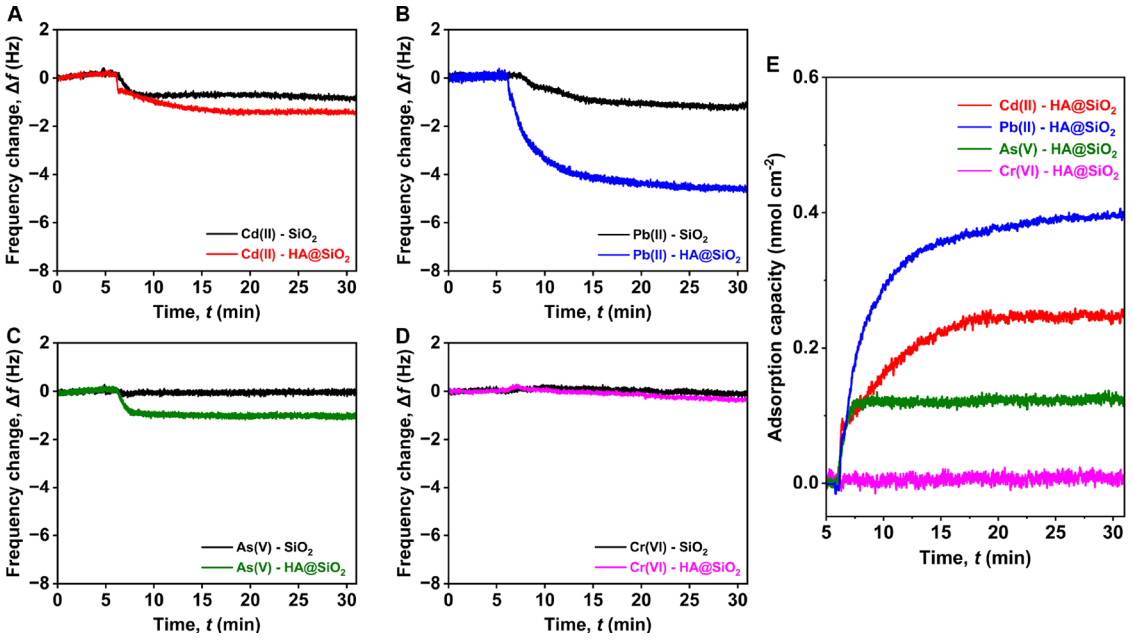

Figure 4. QCM-D adsorption of HMs on bare silica and HA-coated sensors: frequency profiles of (A) Cd(II), (B) Pb(II), (C) As(V), and (D) Cr(VI) adsorption and (E) the corresponding change in the adsorption capacity of HMs on HA-coated sensors.

and 413.6 eV for Cd 3d 3/2, which could be assigned to the binding of Cd(II) with −OH/COOH groups in HA molecules (viz., Cd−O bonding).[33,34] After Pb(II) treatment, the peaks at the binding energies of 137.8 and 138.9 eV for Pb 4f 7/2 as well as 143.1 and 143.8 eV for Pb 4f 5/2 are attributed to the Pb−O bond (Figure 3B).[35,36] In the As 3d spectrum, the obvious peak appears at the binding energy of ∼45.6 eV after As(V) adsorption in Figure 3C, which corresponds to the As−O bonding in arsenate.[37] Due to the low content of As(V) species, the signal-to-noise ratio of the As 3d spectrum is not strong, which further confirms the weak interaction between As(V) and HA molecules. In contrast, the Cr(VI) species could not be detected on the HA surface in the Cr 2p spectrum (Figure 3D), indicating the negligible interaction of Cr(VI) with HA molecules.

FTIR spectroscopy also provides the bonding information between Cd(II)/Pb(II) and HA molecules (Figure S3). Clearly, the C−O symmetric stretching vibration peak at 1382 cm^{-1} is broadened and a new peak at ∼1355 cm^{-1} is generated after Cd(II)/Pb(II) adsorption, both of which correspond to the formation of covalent bond between Cd(II)/Pb(II) and the carboxyl or hydroxyl groups in HA molecules.[38] Interestingly, the antisymmetric stretching vibration peak of aromatic C═C (∼1559 cm^{-1}) is blue-shifted to 1589 cm^{-1} after Pb(II)/Cd(II) adsorption, which is most likely attributed to the cation−π interaction between cationic Pb(II)/Cd(II) and aromatic moieties in HA molecules.[39,40] Compared with Cd(II), the more evident peak at 1589 cm^{-1} for the Pb(II) case may indicate its stronger cation−π interaction. Moreover, the difference between the wavenumbers of the symmetric and antisymmetric peaks (Δ) can be used to determine the type of bonding for metal carboxylate.[41,42] After Cd(II)/Pb(II) adsorption, the Δ value was reduced from ∼200 cm^{-1} for HA molecules to ∼190 cm^{-1} for HA-Cd(II) and ∼175 cm^{-1} for HA-Pb(II), which could be attributed to the bidentate chelating mode.

3.3. QCM-D Adsorption of HMs on HA Surfaces. To compare the adsorption behavior of different types of HMs, the *in situ* adsorption process of HMs on the bare silica and HA-coated sensors was monitored in real time by using QCM-D. Figure 4 shows the frequency shift (Δf) of bare silica and HA-coated sensors during adsorption in 1 mM Cd(II), Pb(II), As(V), and Cr(VI) solutions. On the bare silica surfaces, the Δf value slightly decreases with time upon injection of Cd(II) and Pb(II) solutions, indicating the weak outer-sphere adsorption of Cd(II) and Pb(II) due to the electrostatic attraction between cationic Cd(II)/Pb(II) and negatively charged silica surfaces. In contrast, the electrostatic repulsion inhibits the adsorption of anionic As(V) and Cr(VI) as indicated by the negligible change in the Δf value. It is noted that the HMs solution was injected after the sensors were stabilized in Milli-Q water for a long time, which ensures the effect of HA hydration on the frequency change of QCM-D measurements to be neglected. In the presence of HA, the adsorption of Cd(II) and Pb(II) is significantly enhanced and the adsorption processes involve the fast- and slow-rate regions that ultimately achieve the plateau (Figure 4A,B). The fast adsorption process is attributed to the strong inner-sphere complexation of Cd(II) and Pb(II) with the carboxyl or hydroxyl groups in HA molecules. After the formation of an initial HMs layer, the weak outer-sphere complexation due to the electrostatic attraction results in the slow adsorption process until the adsorption equilibrium is achieved. A small amount of As(V) was adsorbed on the HA surface (Figure 4C), whereas the adsorption of Cr(VI) on the HA surface is very weak (Figure 4D), indicating that anionic Cr(VI) could easily transport through HA-coated soil and a small amount of As(V) may be retained.

Figure 4E shows the change in the adsorption capacity of HMs on the HA surface with time. Since both $\Delta f\, n^{-1}$ and the dissipation changes were a little dependent on the overtone number (3, 5, 7, 9, and 11) in this work, the equilibrated adsorption capacity q_e of the HA surface in 1 mM Cd(II), Pb(II), As(V), and Cr(VI) solutions can be calculated using the Sauerbrey equation and follows the order: Pb(II) (∼0.40 nmol cm^{-2}) > Cd(II) (∼0.25 nmol cm^{-2}) > As(V) (∼0.12

https://doi.org/10.1021/acs.est.3c08309
Environ. Sci. Technol. 2024, 58, 3412−3422

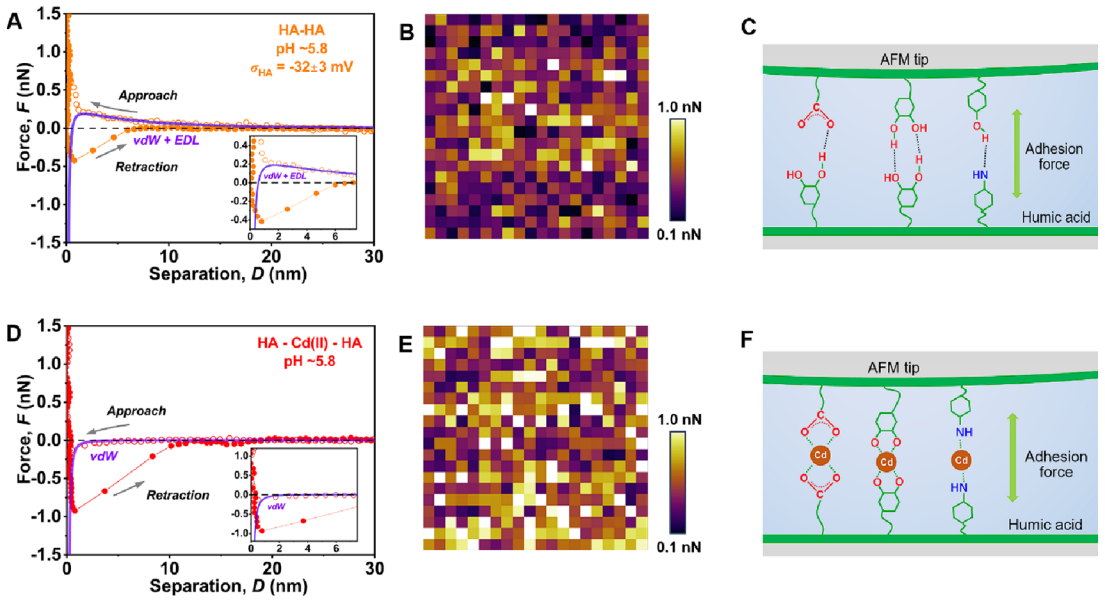

Figure 5. (A, D) Typical force−separation curves between the HA-coated AFM probe and HA surface in the (A) absence and (D) presence of 1 mM Cd(II) at pH ~ 5.8 (measured approach curve: open symbols, measured retraction curve: point-line plot, theoretical fitting results: orange curve, inset: zoomed-in view at short separation, $A_{HA-water-HA}$: 9.28 × 10^{-21} J).[24] (B, D) Adhesion force map of the HA surface (2 × 2 μm^2) measured using the HA-functionalized AFM probe in the (B) absence and (E) presence of Cd(II), and (C, F) corresponding schematic of the binding mechanism.

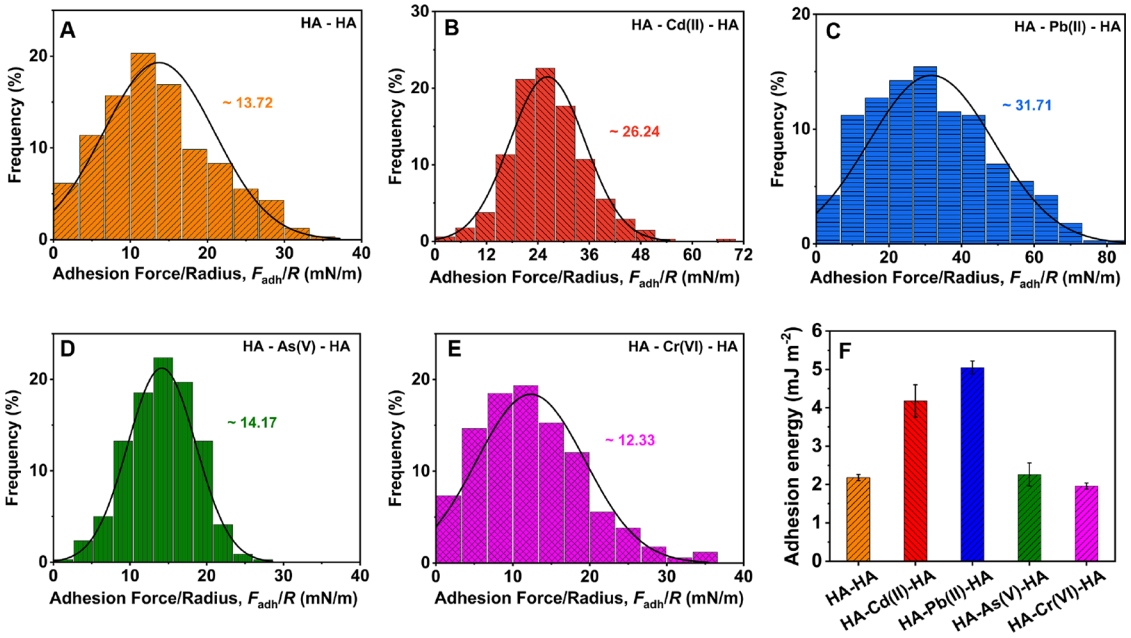

Figure 6. (A−E) The histogram of measured adhesion force F_{adh}/R with the fitted Gaussian distribution between HA surfaces (A) in the absence of HMs and (B−E) in the presence of 1 mM HMs, and (F) the summarization of corresponding adhesion energies for all the cases.

nmol cm^{-2}) > Cr(VI) (~0.02 nmol cm^{-2}). Given $n = q_e \times N_A$ to correlate the equilibrated adsorption capacity q_e to the adsorption density n, the adsorption density of Pb(II) on the HA surface is calculated to be ~2.41 ions nm^{-2}, much higher than ~1.51 ions nm^{-2} for Cd(II), ~0.72 ions nm^{-2} for As(V), and ~0.12 ions nm^{-2} for Cr(VI). Notably, the HA surface exhibits a higher adsorption capacity toward Pb(II) than Cd(II), which could be attributed to the stronger metal−HA complexation and cation−π interactions. In contrast, As(V) could be weakly adsorbed on the HA surface due to the physical interactions such as hydrogen bonding, while the adsorption of Cr(VI) on the HA surface is almost negligible. Moreover, the adsorption of cationic Cd(II) and Pb(II) on the HA surface could be driven by the electrostatic attraction while the electrostatic repulsion suppresses the adsorption of anionic As(V) and Cr(VI).

3.4. Intermolecular Interaction of HA−HMs−HA Systems. The HMs−HA interactions in aqueous media govern the transport and fate of HMs in water-based environments such as soil and surface/underground water. Herein, the interaction forces between HA-functionalized AFM probes and HA surfaces in aqueous solution without

https://doi.org/10.1021/acs.est.3c08309
Environ. Sci. Technol. 2024, 58, 3412−3422

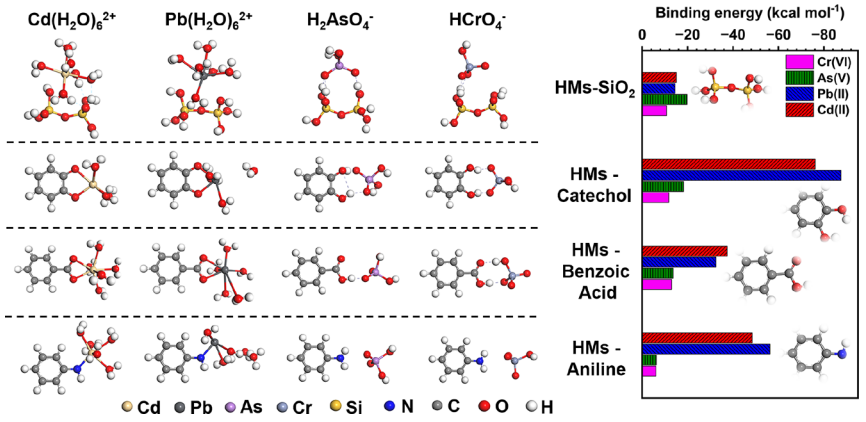

Figure 7. Optimized geometries of $[Cd(H_2O)_6]^{2+}$, $[Pb(H_2O)_6]^{2+}$, $H_2AsO_4^-$, and $HCrO_4^-$ interacting with silica cluster, catechol, benzoic acid, and aniline species (left), respectively, with the corresponding binding energies for all the cases (right).

or with 1 mM Cd(II) at pH 5.8 were quantitatively measured to unravel the Cd(II)-HA interaction mechanism, as shown in Figure 5. In the absence of Cd(II), a long-range repulsion starting from ~23.2 nm is observed during the approach of two interacting HA surfaces (Figure 5A) due to the EDL interaction. By fitting the measured force results with classical DLVO theory, the surface potential of HA is determined to be −32 ± 3 mV at pH 5.8, which agrees well with the previously reported results.[24,25] During the separation of two contacted HA surfaces, the relatively small adhesion force is detected, arising from the weak physical interactions of HA molecules such as hydrogen bonding and vdW interaction. After the Cd(II) addition, the force measured during the surface approach displays a short-range attraction starting from 5.5 to 6.0 nm (Figure 5D), similar to the case of Pb(II) (Figure S4). The weak attractive force is attributed to the vdW interaction, and the EDL interaction could not be detected due to the adsorption of Cd(II) that leads to the electrical neutrality of interacting surfaces. The binding of Cd(II) with HA leads to the enhanced adhesion force between HA molecules due to the HA−Cd(II)−HA bridging effect.

Based on the force−separation profiles measured on 400 consecutive positions in a 2 × 2 μm^2 region, an AFM adhesion force map could be obtained and is demonstrated in Figure 5B,E. The bright/dark region of the adhesion force map indicates the large/small adhesion force. Evidently, the adhesion force map on the HA surface in the presence of Cd(II) is much brighter than the case without Cd(II), revealing the stronger interfacial adhesion between two HA surfaces after the Cd(II) addition. In the absence of Cd(II), the hydrogen bonding between hydrophilic moieties of HA molecules coupled with vdW interaction plays the dominant role in the observed adhesion (Figure 5C). After Cd(II) is introduced, the oxygenated polar groups in HA molecules could bind with Cd(II) to form the HA−Cd(II)−HA complexes, and thus the adhesion is strengthened (Figure 5F).

In addition to the binding of Cd(II), the binding of HA molecules with other HMs could also affect the intermolecular interaction between two HA surfaces. Based on numerous events of measured force−separation profiles, the histograms of normalized adhesion force F_{adh}/R and the fitted Gaussian distributions (solid curve) between HA-functionalized AFM probes and HA surfaces in aqueous solution without or with different types of HMs at pH 5.8 are illustrated in Figure 6. In the absence of HMs, the average normalized adhesion force for the HA−HA system is obtained as 13.72 ± 0.22 mN m^{-1} (Figure 6A). After the addition of cationic HMs, the average adhesion force significantly increases to 26.24 ± 1.25 mN m^{-1} for the HA−Cd(II)−HA system and 31.71 ± 0.52 mN m^{-1} for the HA−Pb(II)−HA system, as shown in Figure 6B,C. In contrast, the presence of anionic HMs has a negligible influence on the interfacial adhesion, with the interaction force of 14.17 ± 0.85 mN m^{-1} for the HA−As(V)−HA system and 12.33 ± 0.21 mN m^{-1} for the HA−Cr(VI)−HA system (Figure 6D,E). Based on the Derjaguin−Muller−Toporov (DMT) model, $W_{adh} = -F_{adh}/2\pi R$, the normalized adhesion force F_{adh}/R can be correlated with the adhesion energy per unit area W_{adh}.[43] The corresponding average adhesion energy follows the trend: Pb(II) (~5.05 mJ m^{-2}) > Cd(II) (~4.18 mJ m^{-2}) > As(V) (~2.26 mJ m^{-2}) > no HMs (~2.18 mJ m^{-2}) > Cr(VI) (~1.96 mJ m^{-2}) (Figure 6F).

Evidently, the large HA−Cd(II)/Pb(II)−HA adhesion force is attributed to the strong binding energy of Cd(II)/Pb(II) with HA molecules, mainly arising from the metal−HA complexation and cation−π interaction. The anionic As(V) could form weak physical interactions (e.g., hydrogen bonding) with HA molecules, similar to the case of HA−HA interaction without HMs, and thus, they almost exhibit the same adhesion energy. Interestingly, the addition of Cr(VI) could slightly reduce the adhesion energy, which is most likely because Cr(VI) that is difficult to bind with HA molecules disrupts the hydrogen bonding network of HA surfaces.

3.5. DFT Simulation of the HMs−HA Binding Mechanism. To further clarify the interaction mechanisms between HMs and HA from the molecular perspective, the binding energies of HMs−HA complexation were calculated using DFT simulation. Based on the Visual MINTEQ model, Cd^{2+}, Pb^{2+}, $H_2AsO_4^-$, and $HCrO_4^-$ are determined to be the predominant species of Cd(II), Pb(II), As(V), and Cr(VI) at pH ~ 5.8 (Figure S5). Moreover, since heavy metal cations exist in the form of hydrates in aqueous solution, the first hydration shell with six water molecules for Cd^{2+}/Pb^{2+} was adopted in DFT calculation.[44] Due to the complex structure of the HA molecule, the typical functional groups in HA molecules (e.g., catechol, benzoic acid, and aniline) was employed to investigate the HMs−HA interaction mechanisms.

The possible adsorption modes of $[Cd(H_2O)_6]^{2+}$, $[Pb(H_2O)_6]^{2+}$, $H_2AsO_4^-$, and $HCrO_4^-$ with the SiO_2 cluster and typical HA species could involve the monodentate complex-

https://doi.org/10.1021/acs.est.3c08309
Environ. Sci. Technol. 2024, 58, 3412−3422

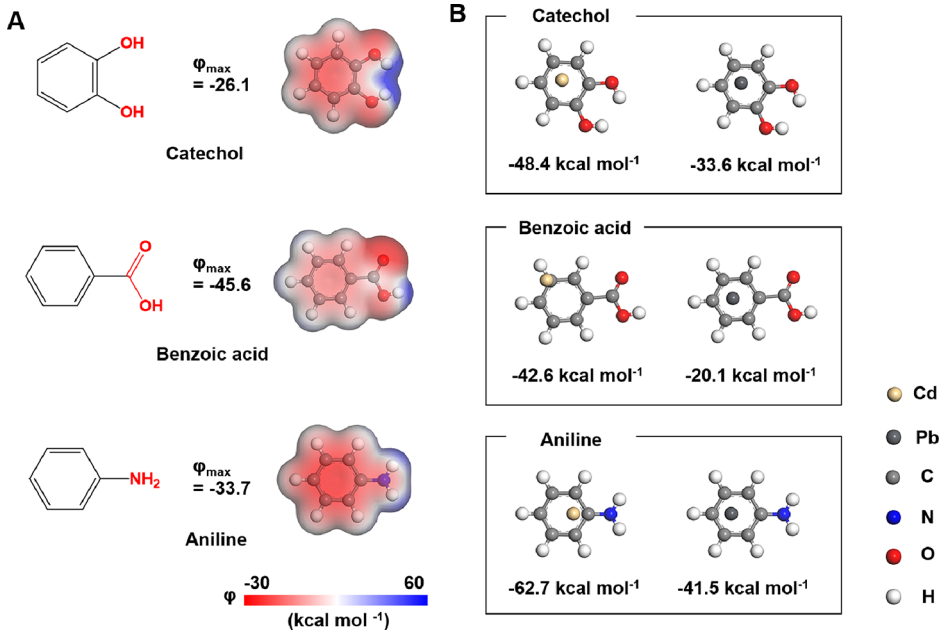

Figure 8. (A) Molecular structure and electrostatic potential (ESP) images of catechol, benzoic acid, and aniline species, (B) and their corresponding cation−π interaction with Cd^{2+} and Pb^{2+}.

ation, bidentate complexation, and outer-sphere adsorption.[45] As shown in Figure 7, $[Cd(H_2O)_6]^{2+}$, $[Pb(H_2O)_6]^{2+}$, $H_2AsO_4^-$, and $HCrO_4^-$ typically exhibit very low binding energy (<20 kcal mol^{-1}) with the SiO_2 cluster via the outer-sphere complexation, which reveals the weak interaction between HMs and silica surfaces. In contrast, the typical HA species prefer to bind with the hydrated Cd^{2+} and Pb^{2+} via the mono- or bidentate complexation while weakly interacting with $H_2AsO_4^-$ and $HCrO_4^-$ via hydrogen bonding, consistent with the QCM-D adsorption and AFM force measurement results.

Notably, the binding energies of catechol, benzoic acid, and aniline groups interacting with the hydrated Cd^{2+} are calculated as −76.1, −37.4, and −48.4 kcal mol^{-1}, respectively, comparable to or lower than the binding energies for the case of hydrated Pb^{2+}, i.e., −87.6, −32.5, and −56.4 kcal mol^{-1} for catechol, benzoic acid, and aniline species, respectively. The difference in the binding energies for the hydrated Cd^{2+} and Pb^{2+} may be due to the higher electronegativity of Pb^{2+} (∼2.33) than Cd^{2+} (∼1.69), which leads to the stronger affinity with HA species for the hydrated Pb^{2+}.[46] Furthermore, the net charge transfer of Pb(II) after the adsorption of HA species is higher than that of Cd(II) (Figure S6), which also contributes to the strong adsorption and retention of hydrated Pb(II) by HA species. It is also noted that the catechol group plays the dominant role in binding with hydrated Pb^{2+}/Cd^{2+} compared to aniline and benzoic acid groups, most likely due to the higher electrostatic potential (ESP) value for the catechol group.[27] For $H_2AsO_4^-$ and $HCrO_4^-$, their binding energies with benzoic acid and aniline species are very low, i.e., −13.6 and −6.3 kcal mol^{-1} for $H_2AsO_4^-$ and −13.0 and −6.1 kcal mol^{-1} for $HCrO_4^-$, which results in difficulty in the retention of As(V) and Cr(VI) in soil. Moreover, the binding energy of catechol species with $H_2AsO_4^-$ is relatively strong (−18.2 kcal mol^{-1}), leading to the slight adsorption of As(V) on the HA surface. Therefore, the catechol group also plays an important role in the binding of HA with heavy metal oxo-anions. Moreover, the binding energies of the alkyl carboxylic acid, alcohol, and amine groups with HMs species are also evaluated (Figure S7). Hexanoic acid, hexyl alcohol, and 1-hexanamine are selected as the model species, and the adsorption energy results are similar to the cases of aromatic species. A stronger hydrogen bonding interaction between As(V) and alkyl species is attributed to the accumulation of charge only at the polar head.

It is interesting to notice that the cation−π interaction between the cationic HMs and the typical aromatic structures in HA molecules also plays an important role in the HMs−HA interaction. As shown in Figure 8A, an abundance of π electrons is distributed in the vertical direction of the π plane of HA species in the ESP images. The π-electron density follows the trend aniline > catechol > benzoic acid, which results in the stronger cation−π interaction between cationic HMs and the aniline group (Figure 8B). The cation−π interaction of the catechol, benzoic acid, and aniline groups of HA molecules with dehydrated Cd^{2+} is significantly stronger than that with dehydrated Pb^{2+}. Notably, the dehydration energy of cationic HMs plays a more important role in determining the cation−π interaction.[47] Generally, the relatively low dehydration energy could facilitate the loss of bound water molecule and the formation of cation−π interaction.[48] Specifically, the lower dehydration penalty for Pb^{2+} indicates the favorable shift from the hydration state to the free ion for Pb^{2+}, thereby allowing Pb^{2+} to easily form the stronger cation−π interaction (Figure S8), which contributes to the enhanced retention of Pb(II) in soil, ultimately leading to the highest HA−Pb(II)−HA adhesion energy in AFM force measurements.

4. ENVIRONMENTAL IMPLICATIONS

The ecological hazards of HMs rely on their mobility and distribution in terrestrial and aquatic environments, which are significantly influenced by naturally occurring HA. To decipher the molecular mechanism underlying the adsorption and retention of HMs by HA, we quantitatively investigated the interactions between HA and different types of HMs (i.e., Cd(II), Pb(II), arsenate, and chromate) at the nanoscale. The

https://doi.org/10.1021/acs.est.3c08309
Environ. Sci. Technol. 2024, 58, 3412−3422

presence of HA on the silica surface plays a key role in mediating the adsorption and retention of cationic Cd(II) and Pb(II) but has a limited effect on the anionic As(V) and Cr(VI) species. Based on QCM-D results, the adsorption capacity of Pb(II) and Cd(II) on the HA surface was measured as ∼0.40 and ∼0.25 nmol cm^{-2}, respectively, much higher than ∼0.12 nmol cm^{-2} for As(V) and ∼0.02 nmol cm^{-2} for Cr(VI). Compared with the interaction between two HA surfaces without HMs, HA−HMs−HA systems displayed distinctly different interaction mechanisms. Specifically, HA−Pb(II)−HA exhibited the strongest adhesion energy (∼5.05 mJ m^{-2}) followed by HA−Cd(II)−HA (∼4.18 mJ m^{-2}), both of which were attributed to the synergistic metal−HA complexation and cation−π interaction. In contrast, As(V)/Cr(VI) could form only weak hydrogen bonding with HA, and thus, HA−As(V)/Cr(VI)−HA displayed very low adhesion energy (∼2.26/∼1.96 mJ m^{-2}). Therefore, cationic HMs such as Cd(II) and Pb(II) are more readily adsorbed on HA-coated soils while anionic HMs such as arsenate and chromate can easily transport through HA-coated soils. These quantitative results also indicate that the mobility of HMs in aquatic environments depends not only on the bonding strength between HMs and substrates but also on the properties of HMs, including charge density, and ionic and hydration radii. This work advances our understanding of the effect of NOM on HMs transport in terrestrial and aquatic environments at the nanoscale and provides the direct intermolecular interaction information underlying the adsorption and retention of HMs in the absence and presence of NOM, which shed light on developing effective strategies to remediate contaminated soils and understanding the biogeochemical cycling of HMs.

■ ASSOCIATED CONTENT

Supporting Information

The Supporting Information is available free of charge at https://pubs.acs.org/doi/10.1021/acs.est.3c08309. QCM-D measurement methods; HA-functionalization methods of AFM probes and substrates; elemental composition of the HA sample; typical molecular structure of HA; water contact angle test results; FTIR spectroscopy of HA before and after Cd(II)/Pb(II) adsorption; typical force−separation approach profiles between the HA-functionalized AFM tip and substrate; species distribution diagrams for 1 mM HMs; net atomic charge transfer of HMs before and after adsorption; and dehydration penalty for hydrated Cd^{2+}/Pb^{2+} (PDF)

■ AUTHOR INFORMATION

Corresponding Authors

Lei Xie − *School of Minerals Processing and Bioengineering, Central South University, Changsha 410083, P. R. China;* orcid.org/0000-0003-3520-4815; Email: lei.xie@csu.edu.cn

Hongbo Zeng − *Department of Chemical and Materials Engineering, University of Alberta, Edmonton, Alberta T6G 1H9, Canada;* orcid.org/0000-0002-1432-5979; Email: hongbo.zeng@ualberta.ca

Authors

Zhoujie Wang − *School of Minerals Processing and Bioengineering, Central South University, Changsha 410083, P. R. China*

Qiuyi Lu − *Department of Chemical and Materials Engineering, University of Alberta, Edmonton, Alberta T6G 1H9, Canada*

Chaopeng Liu − *School of Minerals Processing and Bioengineering, Central South University, Changsha 410083, P. R. China*

Huadong Tian − *School of Minerals Processing and Bioengineering, Central South University, Changsha 410083, P. R. China*

Jingyi Wang − *College of Chemistry and Chemical Engineering, Southwest Petroleum University, Chengdu 610500, P. R. China*

Qi Liu − *Department of Chemical and Materials Engineering, University of Alberta, Edmonton, Alberta T6G 1H9, Canada*

Complete contact information is available at: https://pubs.acs.org/10.1021/acs.est.3c08309

Notes

The authors declare no competing financial interest.

■ ACKNOWLEDGMENTS

We gratefully acknowledge the financial support from the National Natural Science Foundation of China (NSFC k11-372, 22202161), the Natural Science Foundation of Hunan Province (2022JJ30688), the Natural Science Foundation of Sichuan Province (2022NSFSC1239), the Scientific Research Starting Project of SWPU (2021QH2010), the Natural Sciences and Engineering Research Council of Canada (NSERC), the Canada Foundation for Innovation (CFI) and the Canada Research Chairs Program.

■ REFERENCES

(1) Yang, Q.; Li, Z.; Lu, X.; Duan, Q.; Huang, L.; Bi, J. A review of soil heavy metal pollution from industrial and agricultural regions in China: Pollution and risk assessment. *Sci. Total Environ.* **2018**, *642*, 690−700.

(2) Pincus, L. N.; Rudel, H. E.; Petrović, P. V.; Gupta, S.; Westerhoff, P.; Muhich, C. L.; Zimmerman, J. B. Exploring the mechanisms of selectivity for environmentally significant oxo-anion removal during water treatment: a review of common competing oxo-anions and tools for quantifying selective adsorption. *Environ. Sci. Technol.* **2020**, *54* (16), 9769−9790.

(3) Kaur, J.; Sengupta, P.; Mukhopadhyay, S. Critical review of bioadsorption on modified cellulose and removal of divalent heavy metals (Cd, Pb, and Cu). *Ind. Eng. Chem. Res.* **2022**, *61* (5), 1921−1954.

(4) Canfield, R. L.; Henderson, C. R., Jr; Cory-Slechta, D. A.; Cox, C.; Jusko, T. A.; Lanphear, B. P. Intellectual impairment in children with blood lead concentrations below 10 μg per deciliter. *New England Journal of Medicine* **2003**, *348* (16), 1517−1526.

(5) Wang, C.; Luan, J.; Wu, C. Metal-organic frameworks for aquatic arsenic removal. *Water research* **2019**, *158*, 370−382.

(6) Wang, Z.; Tian, H.; Liu, J.; Wang, J.; Lu, Q.; Xie, L. Cd (II) adsorption on earth-abundant serpentine in aqueous environment: Role of interfacial ion specificity. *Environ. Pollut.* **2023**, *331*, 121845.

(7) Zhang, H.; Zhang, R.; Lu, T.; Qi, W.; Zhu, Y.; Lu, M.; Qi, Z.; Chen, W. Enhanced transport of heavy metal ions by low-molecular-weight organic acids in saturated porous media: Link complex stability constants to heavy metal mobility. *Chemosphere* **2022**, *290*, 133339.

(8) Chotpantarat, S.; Kiatvarangkul, N. Facilitated transport of cadmium with montmorillonite KSF colloids under different pH conditions in water-saturated sand columns: Experiment and transport modeling. *Water Res.* **2018**, *146*, 216−231.

(9) Yin, K.; Wang, Q.; Lv, M.; Chen, L. Microorganism remediation strategies towards heavy metals. *Chemical Engineering Journal* **2019**, *360*, 1553−1563.
(10) Zhou, Z.; Zhang, C.; Xi, M.; Ma, H.; Jia, H. Multi-scale modeling of natural organic matter−heavy metal cations interactions: Aggregation and stabilization mechanisms. *Water Res.* **2023**, *238*, 120007.
(11) Kunhi Mouvenchery, Y.; Kučerík, J.; Diehl, D.; Schaumann, G. E. Cation-mediated cross-linking in natural organic matter: a review. *Reviews in Environmental Science and Bio/technology* **2012**, *11*, 41−54.
(12) Wang, D.; Wang, P.; Wang, C.; Ao, Y. Effects of interactions between humic acid and heavy metal ions on the aggregation of TiO2 nanoparticles in water environment. *Environ. Pollut.* **2019**, *248*, 834−844.
(13) Habibul, N.; Chen, W. Structural response of humic acid upon binding with lead: a spectroscopic insight. *Sci. Total Environ.* **2018**, *643*, 479−485.
(14) Li, B.; Liao, P.; Xie, L.; Li, Q.; Pan, C.; Ning, Z.; Liu, C. Reduced NOM triggered rapid Cr (VI) reduction and formation of NOM-Cr (III) colloids in anoxic environments. *Water Res.* **2020**, *181*, 115923.
(15) Fox, D. I.; Pichler, T.; Yeh, D. H.; Alcantar, N. A. Removing heavy metals in water: the interaction of cactus mucilage and arsenate (As (V)). *Environ. Sci. Technol.* **2012**, *46* (8), 4553−4559.
(16) Chen, W.; Huangfu, X.; Xiong, J.; Liu, H.; He, Q. Dynamic retention of thallium (I) on humic acid: Novel insights into the heterogeneous complexation ability and responsiveness. *Water Res.* **2023**, *239*, 120053.
(17) Langner, P.; Mikutta, C.; Kretzschmar, R. Arsenic sequestration by organic sulphur in peat. *Nature Geoscience* **2012**, *5* (1), 66−73.
(18) Jiang, W.; Cai, Q.; Xu, W.; Yang, M.; Cai, Y.; Dionysiou, D. D.; O'Shea, K. E. Cr (VI) adsorption and reduction by humic acid coated on magnetite. *Environ. Sci. Technol.* **2014**, *48* (14), 8078−8085.
(19) Komárek, M.; Koretsky, C. M.; Stephen, K. J.; Alessi, D. S.; Chrastny, V. Competitive adsorption of Cd (II), Cr (VI), and Pb (II) onto nanomaghemite: a spectroscopic and modeling approach. *Environ. Sci. Technol.* **2015**, *49* (21), 12851−12859.
(20) Gutierrez, L.; Nguyen, T. H. Interactions between rotavirus and Suwannee River organic matter: aggregation, deposition, and adhesion force measurement. *Environ. Sci. Technol.* **2012**, *46* (16), 8705−8713.
(21) Aubry, C.; Gutierrez, L.; Croue, J. P. Coating of AFM probes with aquatic humic and non-humic NOM to study their adhesion properties. *Water Res.* **2013**, *47* (9), 3109−3119.
(22) Wang, Z.; Lu, Q.; Wang, J.; Liu, J.; Liu, G.; Sun, W.; Xie, L.; Liu, Q.; Zeng, H. Nanomechanical insights into hydrophobic interactions of mineral surfaces in interfacial adsorption, aggregation and flotation processes. *Chemical Engineering Journal* **2023**, *455*, 140642.
(23) Xie, L.; Gong, L.; Zhang, J.; Han, L.; Xiang, L.; Chen, J.; Liu, J.; Yan, B.; Zeng, H. A wet adhesion strategy via synergistic cation−π and hydrogen bonding interactions of antifouling zwitterions and mussel-inspired binding moieties. *Journal of Materials Chemistry A* **2019**, *7* (38), 21944−21952.
(24) Lu, Q.; Wang, J.; Wang, Z.; Xie, L.; Liu, Q.; Zeng, H. Molecular Insights into the Interaction Mechanism Underlying the Aggregation of Humic Acid and Its Adsorption on Clay Minerals. *Environ. Sci. Technol.* **2023**, *57* (24), 9032−9042.
(25) Xie, L.; Lu, Q.; Mao, X.; Wang, J.; Han, L.; Hu, J.; Lu, Q.; Wang, Y.; Zeng, H. Probing the intermolecular interaction mechanisms between humic acid and different substrates with implications for its adsorption and removal in water treatment. *Water Res.* **2020**, *176*, 115766.
(26) Newcomb, C. J.; Qafoku, N. P.; Grate, J. W.; Bailey, V. L.; De Yoreo, J. J. Developing a molecular picture of soil organic matter−mineral interactions by quantifying organo−mineral binding. *Nat. Commun.* **2017**, *8* (1), 396.
(27) Lu, Q.; Wang, Z.; Wang, J.; Xie, L.; Liu, Q.; Zeng, H. Deciphering the specific interaction of humic acid with divalent cations at the nanoscale. *Chemical Engineering Journal* **2023**, *470*, 144097.
(28) Rios-Carvajal, T.; Pedersen, N.; Bovet, N.; Stipp, S.; Hassenkam, T. Specific ion effects on the interaction of hydrophobic and hydrophilic self-assembled monolayers. *Langmuir* **2018**, *34* (35), 10254−10261.
(29) Zhu, S.; Mo, Y.; Luo, W.; Xiao, Z.; Jin, C.; Qiu, R. Aqueous aggregation and deposition kinetics of fresh and carboxyl-modified nanoplastics in the presence of divalent heavy metals. *Water Res.* **2022**, *222*, 118877.
(30) Dai, C.; Hu, Y. Fe (III) hydroxide nucleation and growth on quartz in the presence of Cu (II), Pb (II), and Cr (III): metal hydrolysis and adsorption. *Environ. Sci. Technol.* **2015**, *49* (1), 292−300.
(31) Lu, Q.; Huang, J.; Maan, O.; Liu, Y.; Zeng, H. Probing molecular interaction mechanisms of organic fouling on polyamide membrane using a surface forces apparatus: Implication for wastewater treatment. *Sci. Total Environ.* **2018**, *622*, 644−654.
(32) Zhang, Y.; Tian, R.; He, A.; Tang, J.; Yang, S.; Li, H. Influence of divalent heavy metals on the aggregation of humic acids: Hofmeister effects. *Chemosphere* **2020**, *261*, 127701.
(33) Yang, F.; Du, Q.; Sui, L.; Cheng, K. One-step fabrication of artificial humic acid-functionalized colloid-like magnetic biochar for rapid heavy metal removal. *Bioresour. Technol.* **2021**, *328*, 124825.
(34) Saha, D.; Barakat, S.; Van Bramer, S. E.; Nelson, K. A.; Hensley, D. K.; Chen, J. Noncompetitive and competitive adsorption of heavy metals in sulfur-functionalized ordered mesoporous carbon. *ACS Appl. Mater. Interfaces* **2016**, *8* (49), 34132−34142.
(35) Luo, J.; Sun, M.; Ritt, C. L.; Liu, X.; Pei, Y.; Crittenden, J. C.; Elimelech, M. Tuning Pb (II) adsorption from aqueous solutions on ultrathin iron oxychloride (FeOCl) nanosheets. *Environ. Sci. Technol.* **2019**, *53* (4), 2075−2085.
(36) Luo, X.; Yuan, J.; Liu, Y.; Liu, C.; Zhu, X.; Dai, X.; Ma, Z.; Wang, F. Improved solid-phase synthesis of phosphorylated cellulose microsphere adsorbents for highly effective Pb2+ removal from water: batch and fixed-bed column performance and adsorption mechanism. *ACS Sustainable Chem. Eng.* **2017**, *5* (6), 5108−5117.
(37) Kumar, A.; Kumar, M.; Singh, B. P. Fabrication and characterization of magnetron sputtered arsenic doped p-type ZnO epitaxial thin films. *Appl. Surf. Sci.* **2010**, *256* (23), 7200−7203.
(38) Wang, N.; Li, B.; Qiao, F.; Sun, J.; Fan, H.; Ai, S. Humic acid-assisted synthesis of stable copper nanoparticles as a peroxidase mimetic and their application in glucose detection. *J. Mater. Chem. B* **2015**, *3* (39), 7718−7723.
(39) Li, A. Y.; Deng, H.; Jiang, Y. H.; Ye, C. H.; Yu, B. G.; Zhou, X. L.; Ma, A. Y. Superefficient removal of heavy metals from wastewater by Mg-loaded biochars: Adsorption characteristics and removal mechanisms. *Langmuir* **2020**, *36* (31), 9160−9174.
(40) Xie, Y.; Zhou, G.; Huang, X.; Cao, X.; Ye, A.; Deng, Y.; Zhang, J.; Lin, C.; Zhang, R. Study on the physicochemical properties changes of field aging biochar and its effects on the immobilization mechanism for Cd2+ and Pb2+. *Ecotoxicology and Environmental Safety* **2022**, *230*, 113107.
(41) Deacon, G.; Phillips, R. Relationships between the carbon-oxygen stretching frequencies of carboxylato complexes and the type of carboxylate coordination. *Coord. Chem. Rev.* **1980**, *33* (3), 227−250.
(42) Sutton, C. C.; da Silva, G.; Franks, G. V. Modeling the IR spectra of aqueous metal carboxylate complexes: Correlation between bonding geometry and stretching mode wavenumber shifts. *Chem. - Eur. J.* **2015**, *21* (18), 6801−6805.
(43) Israelachvili, J. N. *Intermolecular and surface forces*. Academic press: 2011.
(44) Bhattacharjee, A.; Pribil, A. B.; Lim, L. H. V.; Hofer, T. S.; Randolf, B. R.; Rode, B. M. Structural and dynamic aspects of hydration of HAsO4− 2: an ab initio QMCF MD simulation. *J. Phys. Chem. B* **2010**, *114* (11), 3921−3926.
(45) Ma, J.; Luo, J.; Liu, Y.; Wei, Y.; Cai, T.; Yu, X.; Liu, H.; Liu, C.; Crittenden, J. C. Pb (II), Cu (II) and Cd (II) removal using a humic

https://doi.org/10.1021/acs.est.3c08309
Environ. Sci. Technol. 2024, 58, 3412−3422

substance-based double network hydrogel in individual and multi-component systems. *Journal of Materials Chemistry A* **2018**, *6* (41), 20110−20120.
(46) Ma, J.; Xia, M.; Zhu, S.; Wang, F. A new alendronate doped HAP nanomaterial for Pb2+, Cu2+ and Cd2+ effect absorption. *Journal of Hazardous Materials* **2020**, *400*, 123143.
(47) Qu, X.; Wang, X.; Zhu, D. The partitioning of PAHs to egg phospholipids facilitated by copper and proton binding via cation-π interactions. *Environ. Sci. Technol.* **2007**, *41* (24), 8321−8327.
(48) Qu, X.; Liu, P.; Zhu, D. Enhanced sorption of polycyclic aromatic hydrocarbons to tetra-alkyl ammonium modified smectites via cation− π interactions. *Environ. Sci. Technol.* **2008**, *42* (4), 1109−1116.

https://doi.org/10.1021/acs.est.3c08309
Environ. Sci. Technol. 2024, 58, 3412−3422